Andreas Eich (Autor)

Manipulation of Topological Edge States

How Stoichiometric Changes and Surface Manipulation Influence the Dirac Cone of Topological Insulators

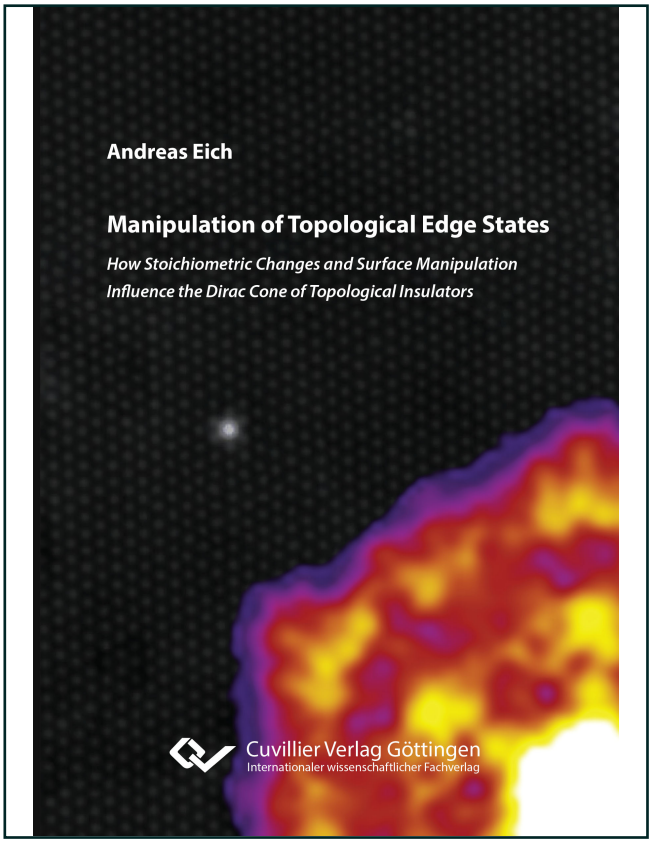

https://cuvillier.de/de/shop/publications/7026

1. Introduction

In the last 40 years the driving force of human progress was the so called *digital revolution*. The term describes the change from an analog to a digital technology initiated by the availability of digital computers and recording to a wider public. It is powered by a constant improvement of speed and complexity of its key technologies. Fundamental was the ability to downsize the basic building blocks, i.e. the transistor used for processing [1, 2] and magnetic areas used for recording [3]. Downsizing allowed to massively increase the number of basic blocks, while at the same time the absolute size of devices, their energy consumption and price remained constant (or even decreased). Because of this stability, it was possible to fully transfer the technological advancements to commercial products, e.g. the transistor count of microprocessors[1] doubled every two years from its invention in the year 1971 until today[2]. It was this dynamic development, that made computers affordable for every household and allowed the incorporation of microprocessors to almost any other existing technology, e.g. cars, telephones, even washing machines. Between 1986 and 2007 general purpose computational capacity grew by 58 % per year, from 0.06 million instructions per seconds and capita to 968 million. Storage capacity jumped from 539 MB to 44716 MB with a digital share of 0.8 % in 1986 and 94 % in 2007 [6].

The basic functionality of microprocessors and hard disk drives (HDD), the dominant recording device, did not change in that time. Microprocessors depend on the ability of transistors to switch and amplify electron currents. HDDs depend on the ability of domains of magnetic material to be stably magnetized in opposite directions and on read/write heads to access the stored information via magnetic fields. Downsizing was enough to keep the growth rate stable[3]. However, it is foreseeable that the used technologies reach their limits. Some of these limits are related to the technologies themselves, e.g. the switching rate of the used transistors or the usability of magnetic fields to access information of a HDD[4].

[1] A microprocessor contains the whole infrastructure needed to carry out a general computer program on one chip. It was this integration that allowed the simultaneous fabrication of the whole infrastructure independent of its complexity and is fundamental for the downsizing effect to deploy its full impact.

[2] The first microprocessor, the Intel 4004, had a transistor count of 2300 [4], the recently released Apple A8X has a count of more than three billion [5].

[3] It has to be mentioned though, that downsizing became only possible by the application of new materials and effects, e.g. the giant magnetoresistance effect for recording heads of HDDs [7, 8]

[4] When the size of a nanoparticle is decreased, its anisotropy constant per atom has to be increased to achieve a similar magnetic stability. Therefore, also the strength of the magnetic field has to be increased. But at smaller dimensions also the power available to create the field is reduced. At some point the saved data cannot be accessed anymore [9].

Other limits are more fundamental. The smallest connection between source and drain of a transistor is an atom [10]. When (and if) such a transistor is realized in commercial products, a further downsizing will not be possible.

Without downsizing more complex microprocessors and storage devices will grow in size, consume more energy and produce more heat (which again compromises the functionality). The production and running costs will increase. More powerful devices will be unaffordable for, at least, the consumer market. If no new driving forces can be found, i.e. new concepts of processing, the tremendous growth described before will come to an end.

But there are proposals on how traditional concepts can be replaced. The use of *spintronics* is maybe the most promising route. While the regular electronics described above utilizes charge transfer to carry and process information, in spintronics also the electron spin is utilized. Spin current based transistors may allow faster and more energy efficient information processing [11]. The spin-torque effect allows spin currents to switch magnetic domains and therefore makes HDD recording heads dispensable [12]. Furthermore, spintronics might allow the creation of qubits that would enable quantum computation [13, 14], a complete new concept of computation, which promises to be extremely fast.

The idea of spintronics has been discussed for quite some time now. In fact, a spin dependent field effect transistor was proposed already in 1990 [15], but most spintronic devices are far from being realized in commercial products[5]. One main issue of spintronics is the reliable creation of spin polarized currents. While these were already achieved and processed at low temperatures by several approaches [16–18], none of these are applicable for devices working at room temperature. Here, the new material class of topological insulator (TI)s [19–22], predicted in 2004 [23–26] and experimentally confirmed in 2007 [19, 27, 28], comes into play, which might solve the problem.

TIs are bulk insulators but with spin-polarized states, that close the band gap at the edge of the material. With a large enough gap, e.g. in Bi_2Se_3 [29], a 100 % spin-polarized current is carried at the surface by the edge states, also at room temperature. Moreover, the peculiar locking of spin and momentum predicted for these states results in complete quenching of direct backscattering.

The correct prediction of TIs is a great achievement of theoretical physics and has led to a new classification system of quantum phases for physical bodies: based on topology. The edge states are a result of a transition between two different topological classes, which is why they exhibit this increased stability concerning perturbations, called topological protection. Their unique properties, spin-polarization, topological protection and linear dispersion, may not only allow the reliable generation of spin currents, but the realization

[5] The only exception are spin valves based on the before mentioned giant magnetoresistance effect.

of new Quantum Hall Effects [30–32], a new type of magneto-electric-effect [33, 34] and the creation of magnetic monopoles [35] or qubits [36]. For this reason TIs are of tremendous interest. And research in this field exploded, especially since the first 3D TI got discovered in 2009[6] [28].

However, research on TIs just started and many questions need to be answered before TIs can be utilized for one of the given purposes. While TIs and the concept of topology are quite well described from a theoretical point of view, many predictions still have to be tested by experiment. Especially the consequences of topological protection have to be further investigated: To what degree are the edge states and their spin-polarization protected concerning different types of perturbations? Do they react? And if so, of what type of reaction is it? Answering these questions will not only sharpen the understanding of the topological concept but will help to find methods of manipulation to fit the properties of a given TI to a certain application. It is the aim of this thesis to contribute to both fields of interest.

The thesis is split in two parts, a theoretical and an experimental part. The theoretical part provides all the information needed to understand the results of the described experiments. It introduces the measurement techniques used, scanning probe methods (SPM) (chapter 2) and photoelectron spectroscopy (chapter 3). Here, the focus is on the scanning probe methods, as these were the main probes for the thesis. An overview on topological insulators is given (chapter 4), including an introduction on the concept of topology, a description of the origin of the edge states and the mechanism behind their protection. The theoretically predicted behavior of the topological edge states (TES) when exposed to perturbations is discussed and a closer look on applications is provided. Furthermore, the properties and the TES behavior of the prototypical TIs Bi_2Se_3 and Bi_2Te_3 are presented, as these are key samples used in this thesis.

The experimental part provides the setup of the scanning tunneling microscope (STM) used for this work (chapter 5) and the results of the conducted experiments. The STM was designed and constructed by myself during the first part of my thesis. It follows the variable temperature STM (VT-STM) design that allows a fast exchange of samples but is optimized concerning stability. Both properties, speed and stability, were crucial for the conducted experiments.

The first experiment (chapter 6) deals with the question how magnetic moments can be introduced to the vicinity of the TES by surface deposition without an extra doping effect, using the example of Fe atoms deposited on Bi_2Se_3. Due to the small density of electron

[6] TI related publications in 2008: 11, 2009: 56, 2013: 879 according to a Web of Science search on the key word "topological insulator" [37].

states around the Fermi level, TIs are very sensitive to surface doping, which induces a large band bending at the edge. This not only shifts the Fermi level, but introduces quantum well states that might interact with the TES and decrease the total spin-polarization of a given current. Here, the consequences of a diffusion of Fe atoms into the surface are investigated by scanning tunneling microscopy (STM), angle resolved photoemission spectroscopy (ARPES) and density functional theory (DFT) calculations.

The chapter concerning the characterization of $PbBi_4Te_7$ (chapter 7) explores the possibility to adjust the bulk band gap as well as the shape and location of the TES bands of binary chalcogenides, such as Bi_2Te_3 and Bi_2Se_3, by changing the crystal composition with group IV elements. Here, Bi_2Te_3 is modified by adding Pb, leading to extra Pb and Te layers within the original crystal structure. The sample is characterized in real and in k-space, using STM and ARPES, the results are compared to theoretical predictions.

On $TlBiSe_2$, the TES response to a heavily disturbed surface is investigated (chapter 8). $TlBiSe_2$ samples are cleaved, a process that rips apart the top layer of the new surface. The surface morphology is studied by STM and atomic force microscopy (AFM), the consequences for the electronic structure are investigated by x-ray photoemission spectroscopy (XPS) and ARPES.

In the final experimental chapter (chapter 9), the hybrid TI Bi-bilayer on Bi_2Se_3 is studied for two reasons. The TES of the substrate is supposed to vertically shift to the new surface, which isolates the edge state from Bi_2Se_3 bulk states. Moreover, the bilayer hosts intrinsic states that might interact with the bulk TES. This interaction as well as the bulk TES location is investigated.

The second reason is the topological nature of the bilayer itself. A freestanding Bi-bilayer is predicted to be a 2D TI with 1D TES, that are sharply localized at the edge [38, 39]. However, the hybridization with substrate states has so far closed the bilayer band gap for all used substrates [40, 41]. The relatively small lateral lattice constant of Bi_2Se_3 may lead to an increased van-der-Waals gap between bilayer and Bi_2Se_3 and therefore to a reduced hybridization. By investigating the final band structure, also the gap size of the bilayer should be unraveled. The first section of the chapter is concerned with a growth study to proof bilayer growth of Bi on Bi_2Se_3. Then the band structure is investigated by ARPES and DFT. In the third section the interaction of surface bands is investigated by an analysis of quasi-particle interference (QPI) patterns on the surface via Fourier transformed STS maps and a simulation of these maps based on the DFT-band structure. By a comparison of q-vectors from theory and experiment all present scattering channels (and therefore bands) at the surface are identified.

For every project presented in this thesis it was necessary to collaborate with different research groups, that provided their unique expertise to unravel all properties of each sample. Since each sample system can only be completely understood by the combination of all experimental and theoretical efforts, I chose to present not only the data measured by myself, but included the results of each part of the collaborations. In the beginning of each chapter I describe who contributed which result. The final conclusions of each experiment are a result of multiple discussions between all collaboration partners.

Part I.

Theoretical Basics of STM, PES and TIs

2. Scanning Tunneling Microscopy

The invention of STM by Binnig and Rohrer in 1982 [42] introduced a unique approach to investigate the surfaces of conductive materials. For the first time it was possible to map surfaces in real space with atomic resolution. In order to gain such a high resolution, a metallic probe is scanned over the sample close enough, that electrons can tunnel between probe and sample. The tunneling current (I) depends strongly on the probe-sample distance and on the local electronic density of states (LDOS) of the sample. By recording the variations of the tunneling current, a map of the surface is achieved, that, to first approximation, resembles the topography of the sample surface. Additionally, the dependency on the sample electron LDOS furthermore enables spectroscopic investigations of the surface electronic structure [43, 44].

The high lateral resolution, as well as the ability of atom manipulation [45] and the fact that the samples are typically not destroyed during measurement, makes scanning tunneling microscopes and derived devices a prime tool to create and characterize nano-structures [46, 47], molecules [48], atoms [49] and even biological systems [50, 51]. The characterization not only includes morphology and electronic structure, but magnetic structure [52], as well as environmental [53] and time dependencies [54, 55].

The intent of this chapter is to give an introduction to STM so far to understand the results of this thesis and the challenges to obtain those. A brief description on the basic STM setup is followed by a section on the fundamental effects and models used to describe the tunneling junction. Finally, the measurement techniques used for this work are described. For a wider overview the books of R. Wiesendanger [56], J. Chen [57] are recommended.

2.1. Basic STM-Setup

In order to measure clean, high resolution images of a sample surface, the sample has to be scanned by a small probe with extreme precision and in a stable environment. Fig 2.1 illustrates the basic setup for STM measurements. The probe is a sharpened metal wire called tip with an apex that is formed ideally by a single atom. It is attached to a scanner made out of a piezoelectric material. By applying a voltage, the scanner can be stretched, compressed or bent with sub-nanometer precision. For this, the scanner is covered with 5 electrodes, +x/-x, +y/-y and z.

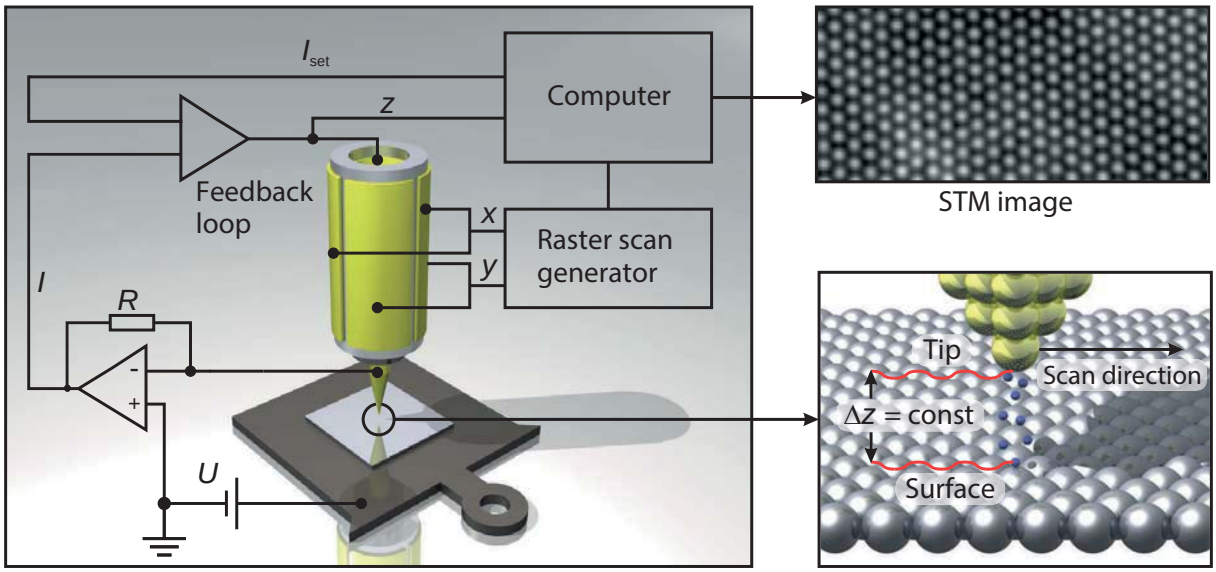

Figure 2.1.: Basic STM Setup A DC voltage U_B is applied between the sample and the tip of the microscope. Due to quantum-mechanical tunneling a current flows through the vacuum barrier (lower image on the right). The current is detected by an I/V-converter. The output signal is sent through a feedback loop to a computer. The tip is installed on a piezo tube. By applying a voltage to the electrodes on the tube, the tube is bent and stretched to scan the tip over the sample and to change the tip-sample distance. An STM image is obtained by the adjustments of the tip-sample distance via the feedback loop to keep I constant (constant current mode).

Tip and sample are integrated into an electric circuit. A net tunneling current I is established by applying a so called bias voltage (U_B) to the sample[1]. The resulting I is amplified by a pre-amplifier and then, depending on the measurement mode, directly processed by a computer to generate an STM image or fed into a feedback loop before. The feedback loop is used mainly to adjust the tip position to the topography of the sample. This will be further described in section 2.3.

The current across the tunneling junction is usually rather small, between 10 pA and several nA, and the tip-sample distance is around 5 Å. A change of 1 Å will already alter I by a factor of 10. Due to the strength and sensitivity of I, the STM is sensitive to pm changes in the sample topography. However, the measured signal is also prone to all kind of disturbances, e.g. mechanical vibrations and electrical noise.

To ensure the highest possible stability, STM measurements are typically conducted in protected environments, at ultra-high vacuum (UHV)-conditions[2] and at low temperatures,

[1] Applying U_B to the sample is the standard configuration. In principle, it can be applied to the tip, too.
[2] Besides an enhanced stability, UHV conditions are needed to guarantee a clean sample surface. Most investigated effects are extremely sensitive to surface contamination. Even the rather inert samples investigated for this thesis suffer from contact with residual gases, see section 4.8.

where either the microscope or the hole chamber is damped. Also the STM materials are chosen to reduce the transmission of vibrations and the used cables are isolated from all external and internal electronic perturbations. A closer look on this topic is given in chapter 5 where the experimental setup is described.

2.2. Theory

Fundamental to the understanding of the STM principle-of-operation is the quantum mechanical tunneling process. In this section a description of the process is given, starting with a simple one dimensional model, which is then adjusted to the peculiarities of STM.

1D Tunneling Effect

In Quantum Mechanics electrons of energy E can be described as waves [58]. When approaching a barrier with the potential strength $V_0 > E$, the electrons are either reflected by or tunnel through the barrier. Fig. 2.2 illustrates this process. Here, the black line represents the potential landscape and the blue line represents the electron wave. The momentum of the waves is indicated by arrows.

If the potential is constant in all three regions, the electrons can be described as quasi-free particles and the exact probability densities of the electron wave in either region can be calculated by the Schrödinger equation, leading to:

$$\psi(x) = \begin{cases} e^{ikx} + Ae^{-ikx} & ;\ x < 0 \\ Be^{i\kappa x} + Ce^{-i\kappa x} & ;\ 0 < x < s \\ De^{ikx} & ;\ x > s \end{cases} \tag{2.1}$$

where s is the barrier width, $k = \sqrt{2mE}/\hbar$ and $\kappa = \sqrt{2m(V_0 - E)}/\hbar$.

The electron wave runs towards the barrier in region I and interferes with that part of the wave that gets reflected at the barrier. Since the wave function and its derivative have to be continuous at every point of the system, it cannot drop to zero when it reaches the barrier. Instead it decreases exponentially within the barrier (region II), leading to a non-zero density probability of the electron wave behind the barrier (region III).

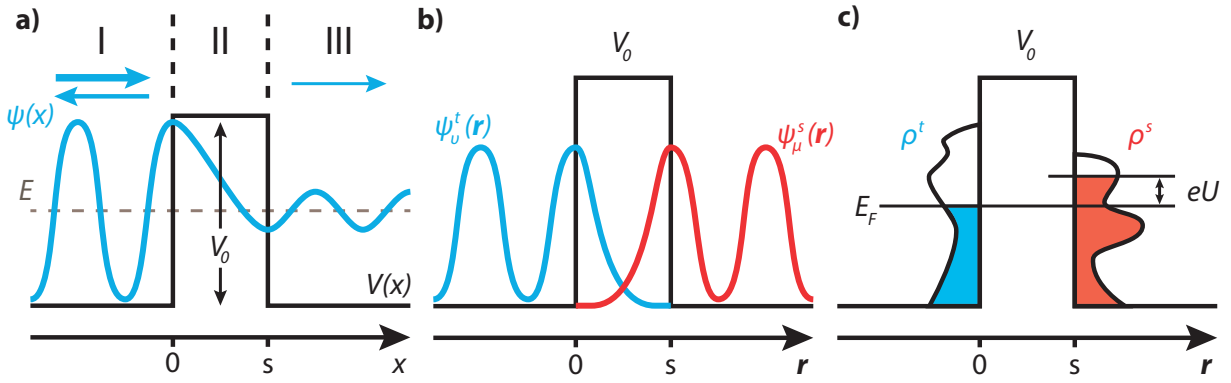

Figure 2.2.: 1D Tunneling Effect and Bardeen Ansatz a) Scheme of the 1D tunneling process at a rectangular barrier of width s and height V_0. An incident electron with energy $E < V_0$ is either reflected by or tunnels through the barrier. In region I and III the electron can be described by a plane wavefunction. Within region II the wavefunction can be described by an exponential decay. The probability density of the wavefunction in III depends on s and V_0. **b)** The Bardeen Ansatz considers two separate systems with known wavefunctions, e.g. ψ_ν^t of the tip and ψ_μ^s of the sample, that overlap in the barrier in between. **c)** I is a convolution of the LDOS of tip ρ^t and sample ρ^s.

Based on the solutions of Eq. 2.1 and the continuity of the wavefunction and its derivative, a transmission coefficient T can be calculated that gives the tunneling probability for the particles for this type of barrier:

$$T = \frac{1}{1 + (k^2 + \kappa^2)^2/(4k^2\kappa^2)\sinh(\kappa s)} \tag{2.2}$$

In case of a strongly attenuating barrier ($\kappa s >> 1$), which is typical for an STM tunnel junction, T can be approximated to:

$$T \approx \frac{16k^2\kappa^2}{(k^2 + \kappa^2)^2} e^{-2\kappa s} \tag{2.3}$$

Hence, T and therefore the tunneling current I, depend exponentially on the barrier width, which explains the high sensitivity to the tip-sample distance mentioned before. While this strong dependence explains the high vertical resolution of scanning tunneling microscopes, a real tunneling barrier is far more complicated than the simple example described here, e.g. the tip and sample exhibit an energy dependent electronic density of states (DOS) and have to be treated in three dimensions, not in 1D. Both aspects have a significant impact on the transmission probability and are considered by a model developed by Bardeen [59].

The Bardeen Ansatz

Bardeen's approach is based on time-dependent perturbation theory and was originally formulated in the 1960s for planar tunnel junctions with superconducting electrodes and insulating oxide layers [60, 61]. However, it can be adopted to calculate the tunneling current I of an STM junction. For this, tip and sample are treated as separate systems, but with an overlap of wave functions within the separating barrier, Fig. 2.2 (b). I is then calculated using Fermi's Golden Rule [58].

The transition rate $\omega_{\mu\nu}$ between an electron state of the tip ψ^t_ν at energy E^t_ν and an electron state of the sample ψ^s_μ at energy E^s_μ is given by

$$\omega_{\mu\nu} = \frac{2\pi}{\hbar} |M_{\mu\nu}|^2 \, \delta(E^t_\nu - E^s_\mu) \tag{2.4}$$

where the δ-function ensures conservation of energy. The associated tunneling matrix element $M_{\mu\nu}$ only depends on the wave functions ψ^t_ν and ψ^s_μ and is given, e.g., by [57] as

$$M_{\mu\nu} = \frac{\hbar^2}{2m} \int_{\mathbf{S}} (\psi^{t*}_\nu \nabla \psi^s_\mu - \psi^{s*}_\mu \nabla \psi^t_\nu) d\mathbf{S} \tag{2.5}$$

where $\mathbf{S}$ is an arbitrary separation surface between tip and sample.

Starting with the transition rate $\omega_{\mu\nu}$, one can calculate the tunneling current I:

$$I = \frac{4\pi e}{\hbar} \sum_{\mu\nu} [f(E^t_\nu - E^t_F) - f(E^s_\mu - E^s_F)] \, |M_{\mu\nu}|^2 \, \delta(E^t_\nu - E^s_\mu) \tag{2.6}$$

where $f(E) = 1/[1 + \exp(E/(k_B T))]$ is the Fermi distribution function. A net tunneling current only arises when a voltage is applied to either tip and sample. If one further replaces the summation over discrete states with the integration of the DOS, equation 2.6 can be written as

$$I(U) = \frac{4\pi e}{\hbar} \int d\epsilon [f(E^t_F - eU_B + \epsilon) - f(E^s_F + \epsilon)] \times \rho^t(E^t_F - eU_B + \epsilon) \rho^s(E^s_F + \epsilon) \left| M(E^s_F + \epsilon, E^t_F - eU_B + \epsilon) \right|^2 \tag{2.7}$$

where ρ^t and ρ^s are the DOS of tip and sample given by

$$\rho_{t,s}(E) \equiv \frac{1}{\epsilon} \sum_{E_n = E - \epsilon}^{E} |\psi_{t,s,n}|^2 \tag{2.8}$$

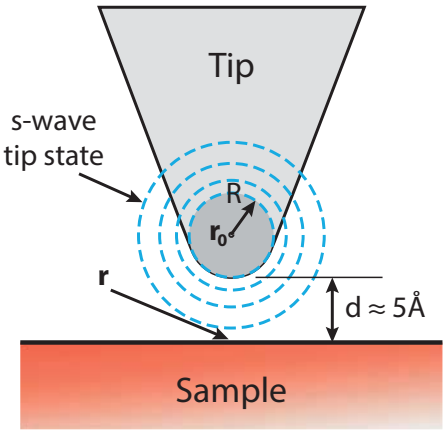

Figure 2.3: Scheme based on the Tersoff-Hamann model. The tip apex is formed by a single atom at position $\mathbf{r}_0$ with a spherical potential well of radius R. The distance of nearest approach is d. The tip-sample distance is given by (R+d). $\mathbf{r}$ depicts the position of the sample surface below the tip. Dotted lines indicate s-wave tip states.

In the temperature limit $T \to 0$ the Fermi distribution becomes a step function and Eq. 2.7 simplifies to

$$I(U_B) = \frac{4\pi e}{\hbar} \int_0^{eU_B} d\epsilon \rho^t(E_F^t - eU_B + \epsilon)\rho^s(E_F^s - \epsilon)\,|M|^2 \tag{2.9}$$

With Bardeen's Ansatz it is theoretically possible to precisely calculate the tunnel current between tip and sample. However, to do so the exact DOS of the sample *and* the tip have to be known. But since the structure of the tip is typically unknown, the same is true for the tip density of states. The unknown tip density of states is not only a theoretical problem. The measured image depends on the DOS of sample and tip. When the influence of the tip is unknown, the origin of the measured features, tip or sample, cannot be identified.

Tersoff-Hamann Model

Fortunately, most experimental data can be reproduced by assuming a specific tip structure, which was introduced by J. Tersoff and D.R. Hamann [62, 63]. Here, the apex exhibits spherical symmetry and is described by s-type wave functions. These are typical of metal tips[3], see Fig. 2.3. Moreover, only small voltages and equal work functions of tip and sample are assumed and the tunneling contact is established at low temperatures.

[3]The model remains valid as long as higher orbital momenta ($l > 0$) have no significant influence on the tunneling current. This also depends on the size of the observed objects. E.g. for metals, Tersoff and Hamann showed that the objects have to be larger than ≈ 3 Å. Fortunately, the lattice constants of all samples measured in the framework of this thesis are much larger than 3 Å. Therefore, metal tips are sufficient to resolve even the smallest details and the Tersoff-Hamann model is adequate to describe the interaction.

With these assumptions the matrix element from Eq. 2.5 can be evaluated and the tunneling current has an extremely simple form. It is proportional to

$$I \propto \sum_{E_\mu^s = E_F - eU_B}^{E_F} \left|\psi_\mu^s(\mathbf{r}_0)\right|^2 = eU_B \rho^s(\mathbf{r}_0, E_F) \tag{2.10}$$

$\rho^s(\mathbf{r}_0, E_F)$ is nothing else but the local electronic density of states (LDOS) of the sample at the position of the tip. Hence, I does not depend on the DOS of the tip any more and the resulting STM image just depends on the tip-sample distance and the sample LDOS.

Model for Higher Bias Voltages

A more general model based on the Wentzel-Kramers-Brillouin (WKB) approximation [44, 64–67] includes also higher voltages. In the temperature limit $T \to 0$ the tunneling current is given by

$$I(U_B) \propto \int_{E_F}^{E_F + eU_B} \mathrm{d}E \rho^t(E - eU_B)\rho^s(\mathbf{r}, E)\mathcal{T}(E, eU_B, d) \tag{2.11}$$

with a transmission coefficient $\mathcal{T}$ described by

$$\mathcal{T}(E, eU_B, d) = \exp\left[-2d\sqrt{\frac{2m_e}{\hbar^2}\left(\frac{\Phi_s + \Phi_t}{2} + \frac{eU_B}{2} - E_\perp\right)}\right] \tag{2.12}$$

where $E_\perp = E - \hbar^2 k_\parallel^2 / 2m_e$ is the component of the electron energy normal to the sample surface, $k_\parallel$ the electron wave vector parallel to the surface and Φ_s and Φ_t are the work functions of sample and tip, respectively. Here, $\rho^s(\mathbf{r}, E)$ is the LDOS of the sample surface at position $\mathbf{r}$ just below the tip apex, see Fig. 2.3.

A closer look on $\mathcal{T}$ reveals two further properties of the tunneling current. Electrons closer to the vacuum level are more likely to tunnel. This is because their wave function decays less strongly within the barrier than tighter bound electrons (see Eq. 2.1). Furthermore, I is dominated by states around $\bar{\Gamma}$ of the surface Brillouin zone (SBZ) with $k_\parallel \to 0$.